Journal of Materials Science: Materials in Electronics (2019) 30:6071–6081
https://doi.org/10.1007/s10854-019-00908-x

Thermo-optical correlation for room temperature synthesis: cold-sintered lead halides

Manish Kumar[1] · Vani Pawar[1] · Priyanka A. Jha[1] · S. K. Gupta[2] · A. S. K. Sinha[3] · Pardeep K. Jha[1] · Prabhakar Singh[1]

Received: 22 October 2018 / Accepted: 7 February 2019 / Published online: 15 February 2019

Abstract

At present, the cost-effective synthesis and stability are major concerns for perovskite halide, which are high-efficient light absorbing solar cell materials. In this work, the cesium lead halides $CsPbX_3$ (where, X = I and Br) were synthesized by simple but unique cold sintering method. The structural (XRD and Raman), microstructural (SEM), electronic (XPS) and optical studies (UV–Visible spectra) revealed that the samples synthesized are in the single phase with P*nma* symmetry. The thermal stability of the samples synthesized was explored by estimating ΔG and ΔS. A negligible change in crystal structure and band gap of the samples is observed after 100 days of synthesis showing the stability of samples in the ambient condition. Along with structure–property correlation, the thermo-optical correlation for halide materials has also been established. A comparative of the band gap (on the basis of synthesis technique) suggests the samples synthesised by cold sintering are at par with other synthesis technique.

1 Introduction

Our world is in need of replacement of conventional energy resources such as coal, petroleum with renewable energy resources such as solar and wind. Solar energy is the most abundant source of renewable energy. Hence, in the last decade, solar cell materials have been intensively studied. One of the critical parameters for a material to be selected for solar cell application is durability (~25 years). The materials known for practical solar cell applications are still based on silicon technologies. According to present fabrication techniques, a reasonably high quality material with the optimum thickness of a few tens of micrometers show incomplete light trapping (< 31% in 1 µm Si-cell photonic light trapping technique [1]) and parasitic losses that create the hindrance in improving the efficiency upon the current record of 26.1% for crystalline-Si based solar cells [2, 3]. For the increase in efficiency of silicon technology, there is a huge demand for other highly efficient solar cell materials. With this objective, perovskites have attracted researchers due to better photovoltaic and promising optoelectronic properties.

Perovskite lead halides have shown utility as better opto-electronic devices with a band gap in the range of 1.5–2.3 eV due to high absorption coefficient and removal of liquid hole transport layer, in case of dye-sensitized based solar cell materials. The cesium lead halides, $CsPbX_3$ (where, X = I and Br), have gained enormous interest in opto-electronics and photovoltaic applications [4]. Cesium lead halide compounds direct band gap nature and high light absorbing power in the UV and visible range prove their utility for the solar cell applications [4, 5]. These materials are also used in light emitting diodes (LED) [6], photo-detector and energy storage applications [7, 8]. But, the major disadvantage of these materials is that they are too prone to moisture and degrade very fastly. Therefore, in spite of very significant opto-electronic features, stability of these compounds becomes a vital issue to be resolved. This may be the reason why onethird of published articles in 2017 on halide materials were focused on stability issue. To resolve the stability issues, there are various techniques employed to synthesize these materials in air such as solvo-thermal synthesis [9],

✉ Pardeep K. Jha
pardeepjha.jiit@gmail.com

✉ Prabhakar Singh
psingh.app@iitbhu.ac.in

[1] Department of Physics, Indian Institute of Technology (Banaras Hindu University) Varanasi, Varanasi 221005, India

[2] Department of Physics, Banasthali Vidyapeeth, Banasthali, Rajasthan 304022, India

[3] Department of Chemical Engineering, Indian Institute of Technology (Banaras Hindu University) Varanasi, Varanasi 221005, India

quantum dots [10], one-step preparation microwave-assisted [11], low temperature synthesis [12] and solution phase synthesis [13] etc. apart from compositional variation [14, 15]. Hence, it appears necessary to understand why these materials are unstable, and too hard to synthesize in ambient condition. If it is intrinsic instability then it would not have been synthesized through the conventional solid state route (SSR). But, we observed that perovskite halides are nucleated at room temperature just by mixing the precursors and that too in ambient condition, thus there is no need of calcination. The grain growth occurs, after sintering the pellet in the vacuum at 80 °C for 1 h (the synthesis details are provided in the sect. 2). Therefore, this effortless cold sintering method [16, 17] was considered worthwhile to synthesize $CsPbX_3$ (where X = I and Br).

In the present work, the formation of $CsPbI_3$ and $CsPbBr_3$ through cold sintering has been analyzed using thermodynamical parameters ΔG and ΔS. The thermodynamical stability using ΔS is also discussed. For the further verification of the formation of these compounds, structural and optical properties are studied. A thermo-optical correlation between free energy and the band gap is also established for the two perovskite halides. The results obtained in the present work are compared (on the basis of synthesis technique) with the existing literature. In addition, the stability with time and light (1 Sun, AM 1.5 G) has also been studied.

2 Experimental details

2.1 Synthesis of samples

$CsPbBr_3$ and $CsPbI_3$ were prepared by the solid state reaction method at room temperature. For preparing $CsPbBr_3$ and $CsPbI_3$, the powders of CsX (X = I, 99.9% and Br 99.999%, Aldrich) and $PbBr_2$ (98%, Aldrich) were weighed in stoichiometric quantities. For the synthesis of PbI_2, the powders of lead nitrate $Pb(NO_3)_2$ and potassium iodide (KI) were weighed according to their mass ratio. The chemical reaction took place as below.

$$Pb(NO_3)_2 + 2KI \rightarrow PbI_2 + 2KNO_3 \tag{1}$$

$Pb(NO_3)_2$ and KI were mixed with distilled water in two separate beakers. The solution of both beakers heated up to the boiling point on a hot plate with a constant stirring rate of 550 RPM. After that, the solution of $Pb(NO_3)_2$ and KI were mixed in a new beaker and kept for natural cooling. After cooling the solution, the yellow precipitate of PbI_2 was formed; these precipitates were filtered and finally heated in the vacuum oven at 100 °C for 2 h to remove moisture. The powder of CsX (X = I, Br) and PbX_2 (X = I, Br) were mixed (Humidity, 34%) and ground up to 2 h in pestle mortar at room temperature in air. $CsPbBr_3$ and $CsPbI_3$ powders were synthesized using the following Eqs. (2) and (3).

$$CsI + PbI_2 \rightarrow CsPbI_3 \tag{2}$$

$$CsBr + PbBr_2 \rightarrow CsPbBr_3 \tag{3}$$

After grinding, the powders of $CsPbBr_3$ and $CsPbI_3$ were pelletized using a hydraulic press and finally sintered in the vacuum oven at 80 °C for 1 h.

2.2 Characterization

The thermodynamics of the powders obtained has been studied using SHIMADZU DSC-60 plus 230V. The resulting perovskite products were characterized by X-ray diffraction (XRD) technique using Rigaku Miniflex for the identification of phase formation. The diffraction patterns were refined by Rietveld refinement method using FULLPROF suite software. The Raman spectra of perovskite powders were detected by DXRxi Raman imaging microscope by Thermo SCIENTIFIC with the excitation wavelength of 780 nm. The optical absorption spectrum was measured by JASCO V-770 ultraviolet–visible (UV) spectrometer. The X-ray photoelectron spectroscopy (XPS) spectrum was recorded at KRATOS (Amicus model) high-performance analytical instrument utilizing Mg target under 10^{-6} Pa pressure. I–V curve measurement has been performed using Keithley 2450 source meter on exposure to radiation through Science tech solar simulator class: AAA with AM1.5 G filter and higher collimated beam.

3 Results and discussion

3.1 Thermodynamics

Figure 1a, b shows the variation of specific heat (C_V) with temperature for $CsPbBr_3$ and $CsPbI_3$, respectively. From the specific heat graphs, it is observed that in $CsPbBr_3$ and $CsPbI_3$, there are three peaks at ~ 177 K, 252 K and 272 K. The heat loss graphs (shown in inset) depict two peaks in $CsPbBr_3$: one endothermic peak at 175 K and one exothermic peak at 249 K. Similarly, one exothermic large peak is observed in $CsPbI_3$ at ~ 252 K showing that the crystallization of these samples is completed well below room temperature, indicating that room temperature would be the higher temperature for the conversion from amorphous to crystalline substances. Moreover, some small exothermic peaks are also observed e.g. at ~ 275 K in both the compounds apart from major variation at ~ 250 K. The specific heat at ~ 250 K is observed to be higher in $CsPbI_3$ (37 J/mol) than $CsPbBr_3$ (29 J/mol). Figure 1c, d shows the variation of ΔG and ΔS with temperature. In $CsPbBr_3$, value

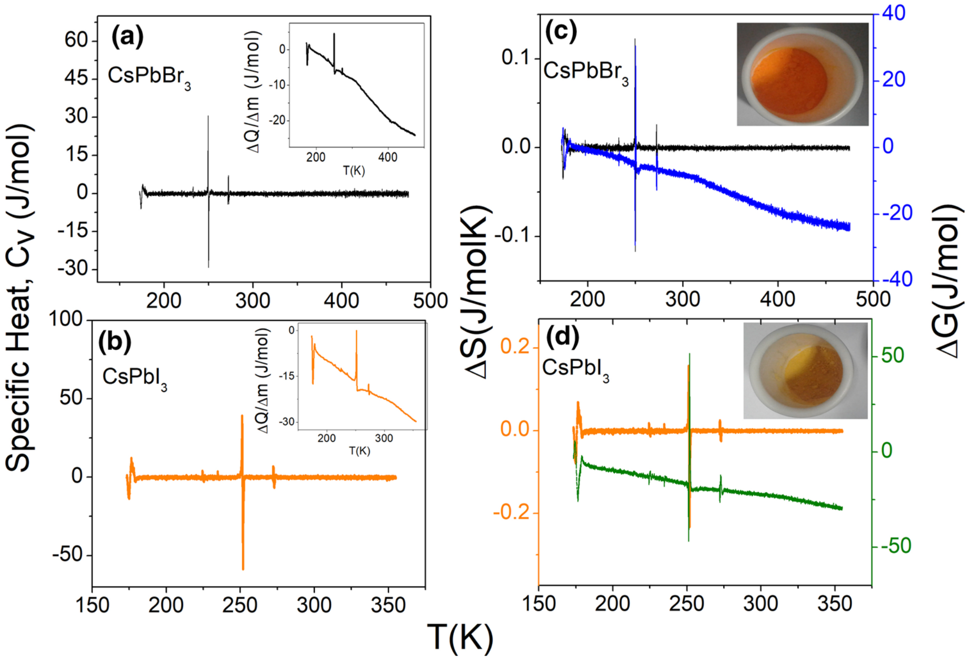

Fig. 1 **a, b** Variation of specific heat (C_V) [insets show variation of (ΔQ/Δm)] and **c, d** variation of change in Gibbs free energy (ΔG) and entropy (ΔS) with temperature for $CsPbBr_3$ and $CsPbI_3$, respectively (insets show respective powder sample synthesized)

of ΔG is −27 J/mol and ΔS is 0.122 J/mol K, whereas, in $CsPbI_3$, value of ΔG is −40J/mol and ΔS is 0.159 J/mol K at 252 K. The higher negative values of ΔG and higher positive values of ΔS favour the product formation well below room temperature more in $CsPbI_3$. In addition to it, there is gradual increase in ΔG for $CsPbI_3$ and $CsPbBr_3$, showing the possibility of forward reaction. In $CsPbBr_3$, the increase in ΔG is steeper than that of in $CsPbI_3$, whereas, entropy is nearly constant showing the thermodynamical stability of the studied samples.

3.2 Structural studies

3.2.1 X-ray diffraction

The phase formation of $CsPbBr_3$ and $CsPbI_3$ was verified by XRD with Cu–Kα radiation ($\lambda = 1.540598$ Å) in the 2θ range of 5°–70° with a step size of 0.01° at room temperature. Figure 2 shows the XRD patterns of $CsPbBr_3$ and $CsPbI_3$ samples. It is observed that XRD of $CsPbBr_3$ and $CsPbI_3$ show the orthorhombic phase with P*nma* symmetry. The comparison of XRD patterns shows that $CsPbI_3$ has more diffraction peaks than that of $CsPbBr_3$. The diffraction peak (121) corresponding to $2\theta \approx 21.53°$ of $CsPbBr_3$ is shifted to lower angle in comparison to the diffraction peak (212) of $CsPbI_3$ corresponding to $2\theta \approx 27.02°$ (as highlighted in Fig. 2 in grey rectangle). It may be attributed to the lattice contraction as I^- (ionic radius 2.2 Å) is larger than Br^- (ionic radius 1.96 Å). This should create more disorder in $CsPbI_3$ sample.

For the strain in the lattice, microstrain and crystallite size have been calculated using the Williamson–Hall (W–H) equation (graphs not shown here).

$$\beta \cos\theta = 0.9\frac{\lambda}{t} + 4\varepsilon \sin\theta \tag{4}$$

where β, λ, ε and θ are the full width at half maximum (FWHM) of the diffraction peak, the X-ray wavelength ($\lambda = 1.54098$ Å), microstrain and Bragg angle of the diffraction peak, respectively. It is observed that the lattice of $CsPbI_3$ ($\varepsilon = 0.09$) is more strained than that of $CsPbBr_3$ ($\varepsilon = 0.03$). The average crystallite sizes of $CsPbBr_3$ and $CsPbI_3$ materials obtained from W–H plots are 102.58 and 60.50 nm, respectively. For further verification of phase formation, the XRD data of these materials are well refined with P*nma* symmetry using FULLPROF software package (Fig. 3) and the lattice parameters; R_{exp}, R_p and R_{wp} etc. obtained after refinement are mentioned in Table 1.

3.2.2 Raman spectroscopy

In order to understand the structure of these samples in depth, Raman measurements were carried out in the wave number range of 50–500 cm^{-1}. The Raman spectra of $CsPbBr_3$ and $CsPbI_3$ were obtained by exciting 780 nm lasers light at the room temperature (Fig. 4). According to the Bilbao crystallographic server, the number of modes for P*nma* symmetry should be 9. On deconvoluting the data, we have observed that the number of modes in $CsPbI_3$ (9) is more than that in $CsPbBr_3$ (7). But the number of modes is less than nine inferring the presence

Fig. 2 Room temperature indexed X-ray diffractograms showing the single phase formation for $CsPbBr_3$ and $CsPbI_3$, respectively. Most intense peak is highlighted in gray rectangle to show change in the XRD pattern with replacement of Br with I

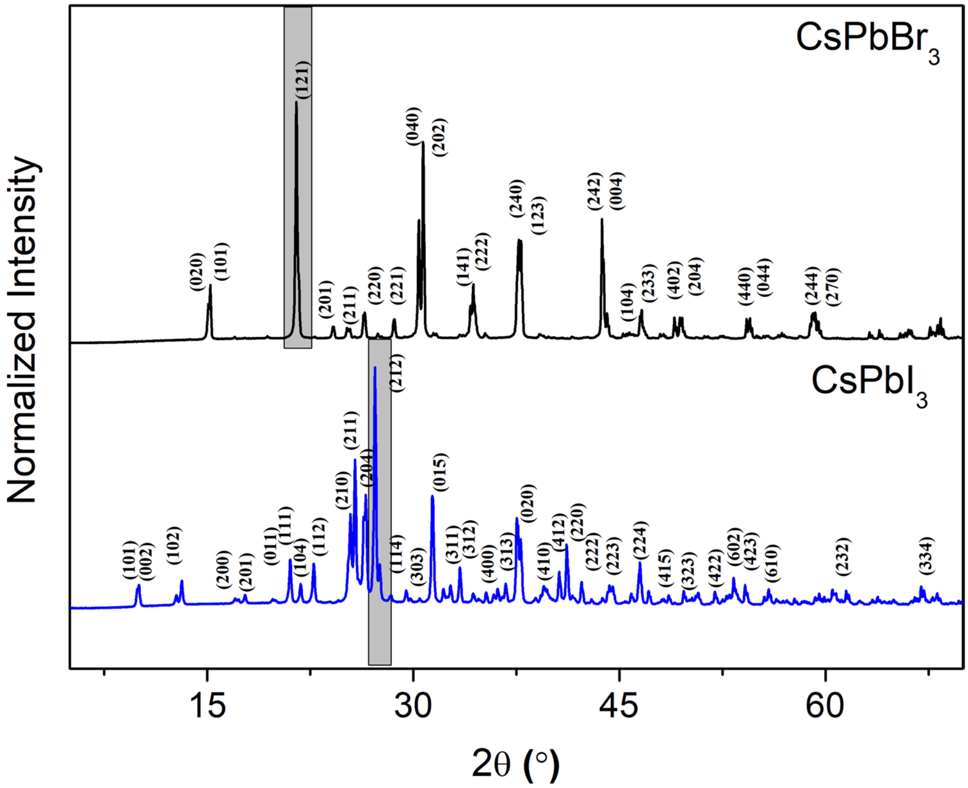

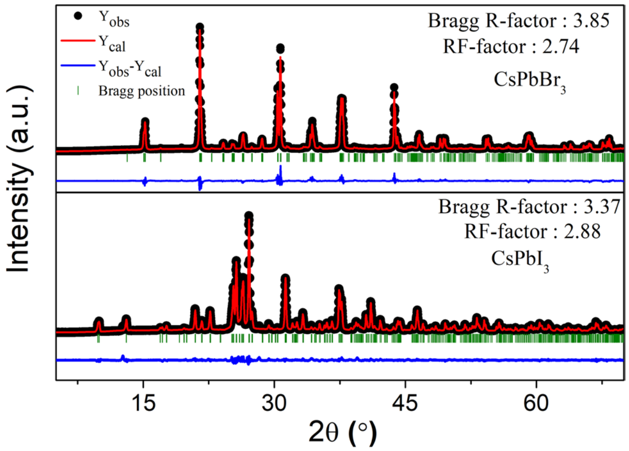

Fig. 3 Rietveld refinement of XRD with the evaluated parameters for $CsPbBr_3$ and $CsPbI_3$, respectively

Table 1 Lattice parameters and fitting parameters for the studied samples

Parameters	$CsPbBr_3$	$CsPbI_3$
Structure	Orthorhombic	Orthorhombic
Space group	P*nma* (62)	P*nma* (62)
Lattice parameters	$\alpha=\beta=\gamma=90°$	$\alpha=\beta=\gamma=90°$
a (Å)	8.261559	10.471622
b (Å)	11.766452	4.804939
c (Å)	8.212267	17.798300
Cell volume (Å^3)	798.3081	895.5330
R_{exp}	2.79	2.71
R_p	6.54	8.99
R_{wp}	6.85	11.4
RF-factor	2.74	2.88
Bragg R-factor	3.85	3.37

of same symmetry. The difference in the number of modes in Raman and number of peaks in XRD are very well correlated. For the number of peaks in XRD pattern, we studied $h^2+k^2+l^2$; there are nearly double reflections observed along the c-axis in the $CsPbI_3$ in comparison to the b-axis orientation in $CsPbBr_3$. This shows the different orientation of the two compounds. In the case of P*nma* symmetry, the modes observed are A_g, B_{1g}, B_{2g} and B_{3g} stretching modes. The A_g and B_g modes correspond to the stretching of Pb–I and Cs–I bonds. The intensity of stretching mode observed at ~ 110 cm^{-1} is higher in $CsPbI_3$ than that of $CsPbBr_3$. In addition to it, the FWHM observed for the band corresponding to ~ 110 cm^{-1} is less in $CsPbI_3$ (19.70 cm^{-1}) than $CsPbBr_3$ (33.42 cm^{-1}). This shows that bonds are more stretched in $CsPbI_3$ in comparison to $CsPbBr_3$.

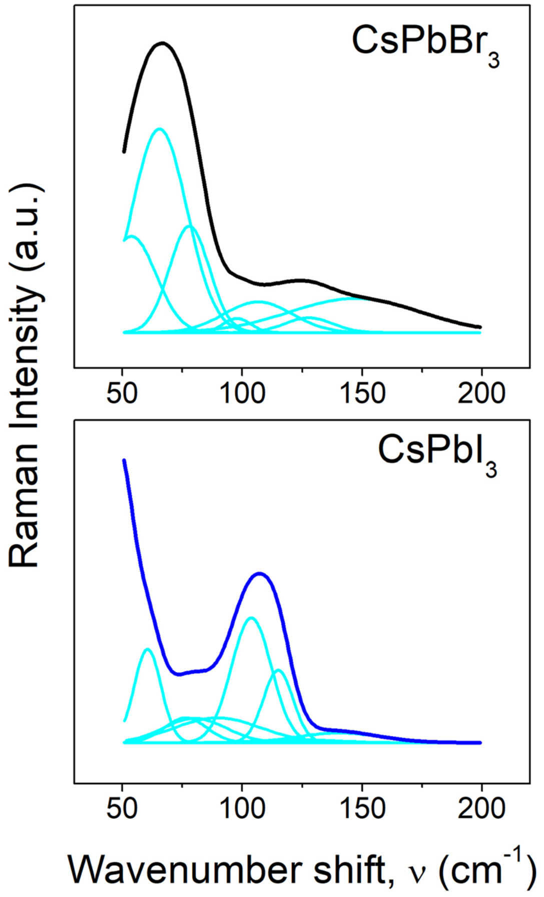

Fig. 4 De-convoluted Raman spectra of $CsPbBr_3$ and $CsPbI_3$ showing the number of modes in agreement with the P*nma* symmetry according to Bilbao crystallographic server

3.3 Microstructural studies

To study the grain morphology and density of the studied samples, SEM micrographs of $CsPbBr_3$ and $CsPbI_3$ are recorded and shown in Fig. 5. It is observed that $CsPbBr_3$ show a large distribution of grains in spherical form with pores. But in case of $CsPbI_3$, the distribution of grains is in the regular form without voids. It is found through grain size distribution histograms (Fig. 5 respective insets) that the average grain sizes of $CsPbBr_3$ and $CsPbI_3$ are 1.90 µm and 0.51 µm, respectively. It can be correlated with the crystallite size as larger crystallites result in larger grains in case of $CsPbBr_3$.

3.4 XPS studies

The XPS spectra of $CsPbBr_3$ and $CsPbI_3$ were analyzed for the constituent's elemental details after calibration with the C 1s peak at 284.5 eV. Figure 6 shows the wide range spectrum to confirm the oxidation state of different ions. All peaks are assigned from the National Institute of Standard and Technology (NIST) XPS database [18]. To confirm the presence of Cs, Pb, I and Br in the powder samples, The most intense photoelectric peaks are observed for Cs $3d_{5/2}$, Cs $3d_{3/2}$, Cs $4d_{3/2}$, Pb $4f_{5/2}$, I $3d_{5/2}$ and Br $3d_{5/2}$. Other low intensity peaks are collected for Cs $4p_{3/2}$, Cs $3p_{3/2}$, C 1s, Br $3p_{1/2}$ and Br $3s_{1/2}$. Further, some auger peaks—Cs auger and Cs loss are also observed. The presence of constituent elements was confirmed in the XPS spectrum of these materials.

Figure 7 shows the deconvoluted comparative elemental XPS spectrum along with the spin–orbit interaction. The presence of $3d_{5/2}$ and $3d_{3/2}$ for Cs, $4f_{5/2}$ and $4f_{3/2}$ for Pb and doublets $3d_{5/2}$ and $3d_{3/2}$ for I^- and Br^- confirms the electronic states. After analyzing the data, a left chemical shift of Cs peaks is observed for $CsPbBr_3$ showing the change in oxidation state of Cs. It is also observed that in the peak corresponding to Cs, there is a formation of a hump in $CsPbI_3$ and can be classified as auger peak. In addition to it, Pb doublets of $4f_{5/2}$ and $4f_{3/2}$ peaks are observed along with the satellite features. In Br^- and I^- spectra, some shake ups are observed leading to the formation of some small peaks [19]. The change in oxidation state indicates the higher binding energy of I^- than that of Br^-. The satellite features observed in Pb indicate the metal–ligand interaction i.e. interaction between Pb and X (= I, Br). Also, the intensity of $4f_{5/2}$ and $4f_{3/2}$ for Pb is swapped in I and Br i.e. the peak having a higher intensity in $CsPbBr_3$ has lower intensity in $CsPbI_3$ or vice-versa.

Fig. 5 SEM micrographs of $CsPbBr_3$ and $CsPbI_3$ samples

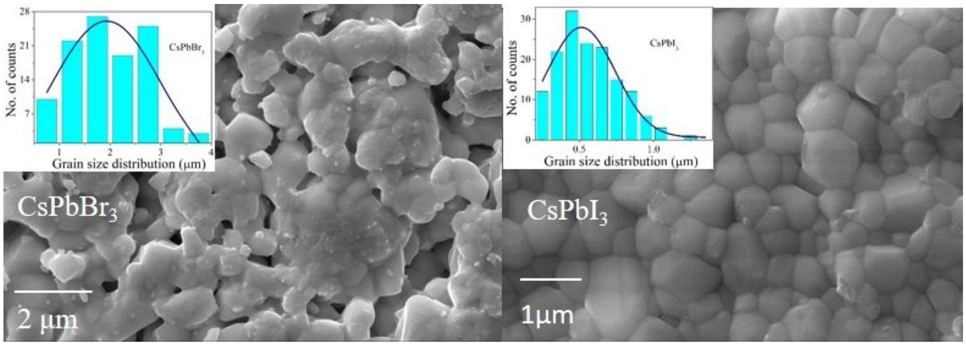

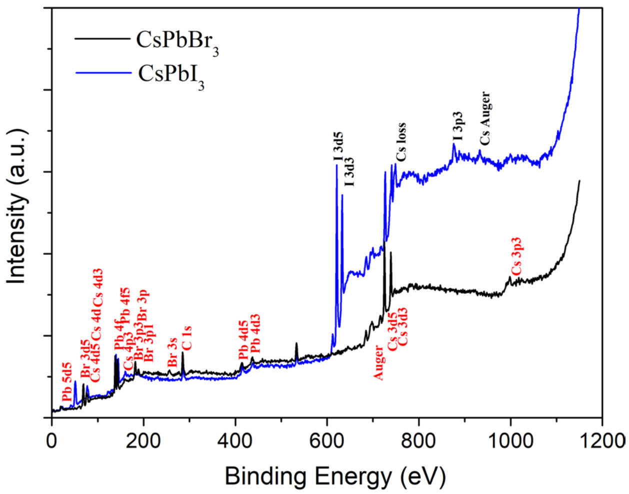

Fig. 6 Wide range XPS spectrum for the confirmation of oxidation states of different constituent elements

3.5 Band gap using UV–Vis

The optical spectrum is obtained in the wavelength region between 250 and 700 nm. In the optical absorption spectrum, (Fig. 8a), a strong absorbance edge at 555 nm is observed for CsPbBr$_3$. But CsPbI$_3$ sample shows two absorbance edges at 501 and 543 nm. It shows that the absorbance edge in CsPbBr$_3$ is shifted towards higher wavelength than that of CsPbI$_3$. To obtain the value of the band gap energy of studied samples, the variation of $(\alpha h\nu)^2$ versus $h\nu$ is plotted (Fig. 8b). It is observed that for CsPbI$_3$, there are two band gaps while there is only one band gap in CsPbBr$_3$. The optical band gap energy (E_g) for these materials is estimated from the intercept with the energy axis and is found to be 2.26 eV for CsPbBr$_3$. In the case of CsPbI$_3$, two band gaps are observed nearly at 2.33 eV and 2.63 eV. This band gap energy change may be attributed to large ionic radii of I$^-$ in comparison to the radii of Br$^-$ [20].

To evaluate the type of band gap, power factor has been evaluated using the well-known relation [21] (Fig. 9).

$$(\alpha h\nu) = A\left(h\nu - E_g\right)^n \tag{5}$$

where α is the absorption coefficient, A is an energy independent constant, E_g is the optical band gap energy, $h\nu$ is the incident photon energy and another constant (n) represents the power factor of transition modes. Taking logarithm on both sides of Eq. (5) and the equation becomes

$$\ln(\alpha h\nu) = \mathrm{n}\ln\left(h\nu - E_g\right) + \ln \mathrm{A} \tag{6}$$

Then, comparing Eq. (6) from the straight line equation y = mx + c. We have obtained the value of slope (m = n), which give the transition modes. To confirm the power factor (n) for direct allowed (n = 1/2), indirect allowed (n = 2), direct forbidden (n = 3/2) and indirect forbidden (n = 3) transitions [22], we have taken the plot of ln $(\alpha h\nu)$ versus ln $(h\nu - E_g)$.

After analyzing the linear curves fitting, we found the values of n. As seen from Fig. 9, CsPbBr$_3$ and CsPbI$_3$ possess the direct allowed transitions as the value of power factor (n) are 0.47 and 0.46, respectively (i.e. close to 0.5).

3.6 Urbach energy

In optical absorption spectra, near band edges have an exponential part called exponential tail (Urbach tail). In

Fig. 7 De-convoluted elemental XPS spectrum along with the spin orbit interaction for CsPbBr$_3$ and CsPbI$_3$

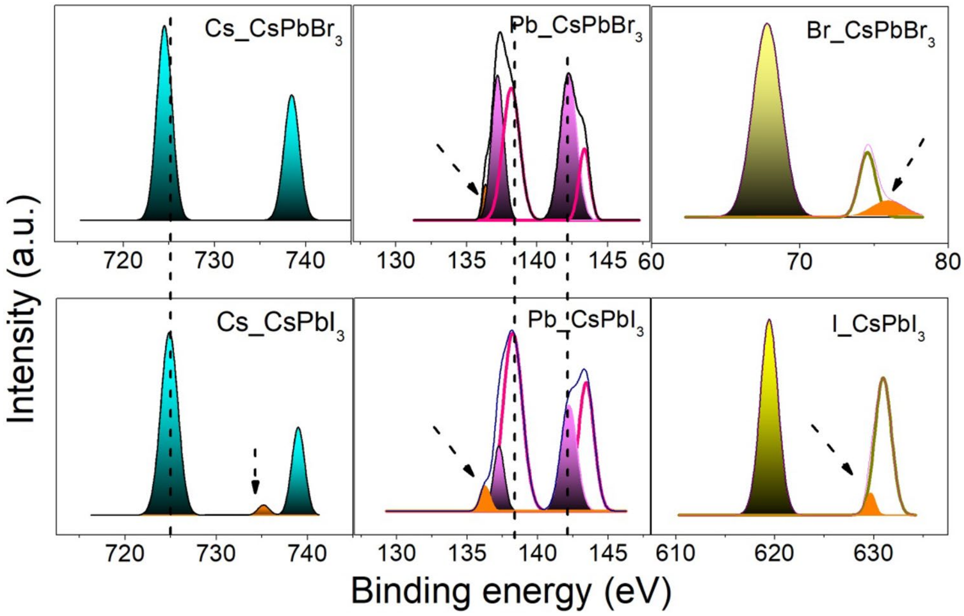

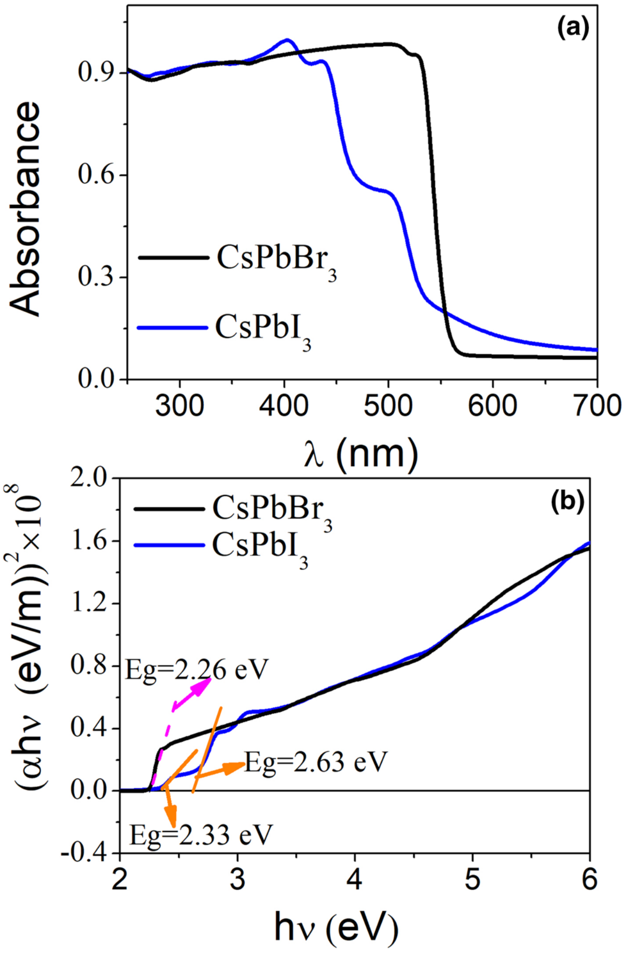

Fig. 8 **a** Optical absorption spectra for $CsPbBr_3$ and $CsPbI_3$, a strong absorbance edge at 555 nm is observed for $CsPbBr_3$ while, on the other hand, for $CsPbI_3$ two absorbance edges at 501 nm and 543 nm are observed, **b** direct band gap energy estimation from Tauc relation for $CsPbBr_3$ and $CsPbI_3$, respectively

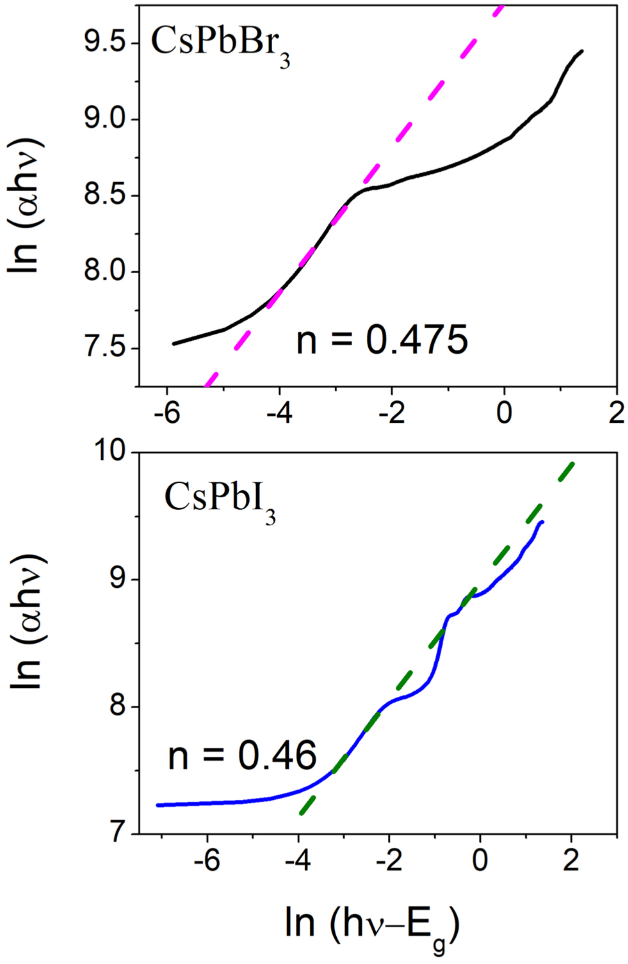

Fig. 9 Direct allowed transitions in $CsPbBr_3$ and $CsPbI_3$

the energy range $E < E_g$, an exponential dependence of the absorption coefficient (α) on photon energy (hν) (Urbach tail) is expressed as [23]:

$$\alpha = \alpha_0 \exp\left(h\nu/E_u\right) \tag{7}$$

where α_0 is a constant and E_u represents the Urbach energy or indicates the energy of the band tail. Taking logarithm both sides of the above Eq. (7)

$$\ln\alpha = \left(h\nu/E_u\right) + \ln\alpha_0 \tag{8}$$

here, Urbach energy is the inverse of the slope of Eq. 8.

Figure 10 shows the plot of ln (α) versus $h\nu$ (eV) for Urbach energy estimation. The value of E_u obtained from the slope (m) of linear fit analysis of these curves for $CsPbBr_3$ is 50 meV and in case of $CsPbI_3$, the values of the Urbach energy obtained are 135 meV and 303 meV corresponding to the band gaps 2.33 eV and 2.63 eV,

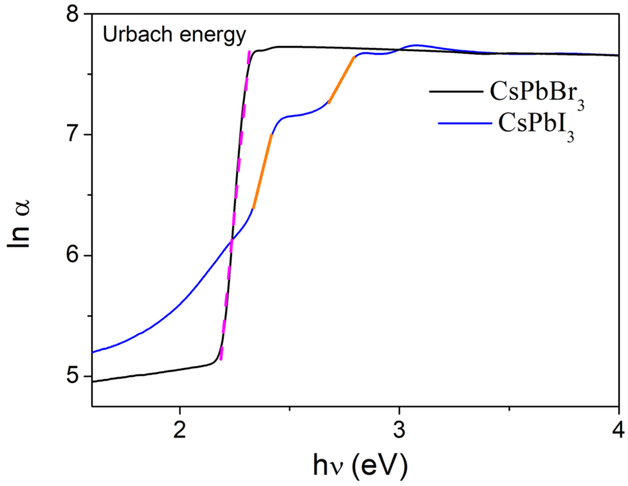

Fig. 10 Plot of ln (α) versus $h\nu$ (eV) for Urbach energy

respectively. The Urbach energy for $CsPbI_3$ is higher than that of $CsPbBr_3$. It is attributed to the perturbation of structural disorder in $CsPbI_3$ and is in correlation with the strain obtained from structure [24].

4 Structure–property correlation and stability

4.1 Structure–optical correlation

It is well known that quantum size of material and defect present in the sample are correlated to optical band gap energy. In the present study, it is observed that $CsPbBr_3$ is having small unit cell volume, but large crystallite and grain sizes. Also, the lattice of $CsPbI_3$ ($\epsilon = 0.09$) is more strained than that of $CsPbBr_3$ ($\varepsilon = 0.03$). The Urbach energy and band gap energy are higher for $CsPbI_3$ than $CsPbBr_3$. The lattice orientation of $CsPbBr_3$ is about b-axis but for $CsPbI_3$, it is more about the c-axis. Although both structure is orthorhombic but in case of $CsPbBr_3$ all lattice constants are larger (> 8 Å) than b_{CsPbI3} (= 4.804939 Å). So, the optical band gap energy is in correlation with the structure and microstructure of materials. The strained matrix generates structural disorder, hence should possess localised states and higher Urbach energy. The strained matrix in $CsPbI_3$ is attributed to the increase in the number of stretching modes in comparison to $CsPbBr_3$. To further verify the structural disorder observed in Urbach energy, we have coupled it with the FWHM of the Raman mode at ~ 110 cm^{-1} which is lower in $CsPbI_3$ (19.70 cm^{-1}) than $CsPbBr_3$ (33.42 cm^{-1}). This decrease in FWHM increases the structural disorder and hence, Urbach energy. The shifting of the peak at ~ 110 cm^{-1} of $CsPbI_3$ increases the strain and hence the band gap has increased in $CsPbI_3$.

4.2 Thermo-optical correlation

The enthalpy obtained from thermodynamics is correlated with the band gap through the empirical relation [25, 26], $E_g = A\exp\left(0.34 \times E_{\Delta H^0}\right)$ where A is a pre-exponential factor, a property of the cation and as reported earlier, value of A is 1.35 for p-block elements, E_g is the band gap and $E_{\Delta H^0}$ is the energy obtained from enthalpy using the following relation

$$E_{\Delta H^0} = -5.22 \times 10^{19}\left(\frac{\Delta H_f^0}{Nne}\right)$$

where ΔH_f^0 (in cal/mol) is the standard enthalpy of the formation of halides, N is Avogadro's number and 'n' is the number of electrons transferred in the reaction and 'e' is the basic electronic charge. $E_{\Delta H^0}$ correspond to the energy levels related to one metal-halide bond in the halide. These relations are used in oxides and found true for halides as well in the present case. In the present case, the ratio of band gap obtained thermodynamically using enthalpy is $\left(\frac{E_{g,Br}}{E_{g,I}} = \frac{\exp\left(0.34 \times E_{\Delta H^0}\right)_{Br}}{\exp\left(0.34 \times E_{\Delta H^0}\right)_{I}} = \right)1.03$ the ratio of band gap obtained from UV–Vis data is 0.96.

4.3 Comparative (on the basis of synthesis techniques) of band gap

The comparative table (Table 2) of band gap energy observed for these two samples synthesized with other significant methods indicates that the value is smallest for the samples prepared by cold sintering.

4.4 Stability

Till now we have seen that the structural and optical properties of compound synthesized by cold sintering are well

Table 2 Comparative (on the basis of synthesis techniques) of structural and optical properties

Material	Synthesis method	Band gap (eV)		References
		$CsPbBr_3$	$CSPbI_3$	
$CsPbBr_3$ and $CsPbI_3$	Solution phase synthesis (nanowires)	2.38	2.71	[13]
$CsPbBr_3$	Transformation doping method (nanocrystals)	2.84	x	[27]
$CsPbBr_3$	Quantum dot	2.39	x	[28]
$CsPbI_3$	One-pot solution spin coating	2.82	x	[29]
$CsPbBr_3$	Facile synthesis	2.35	x	[30]
$CsPbBr_3$	Two-step sequential deposition technique	2.36	x	[31]
$CsPbBr_3$ and $CsPbI_3$	Spin coating	2.3	2.82	[32]
$CsPbI_3$	Thin film by thermal evaporation	x	3.013	[33]
$CsPbBr_3$	Two step-sequential deposition	2.39	x	[34]
$CsPbBr_3$ and $CsPbI_3$	Cold sintering	2.26	2.33	In present work

X—not reported

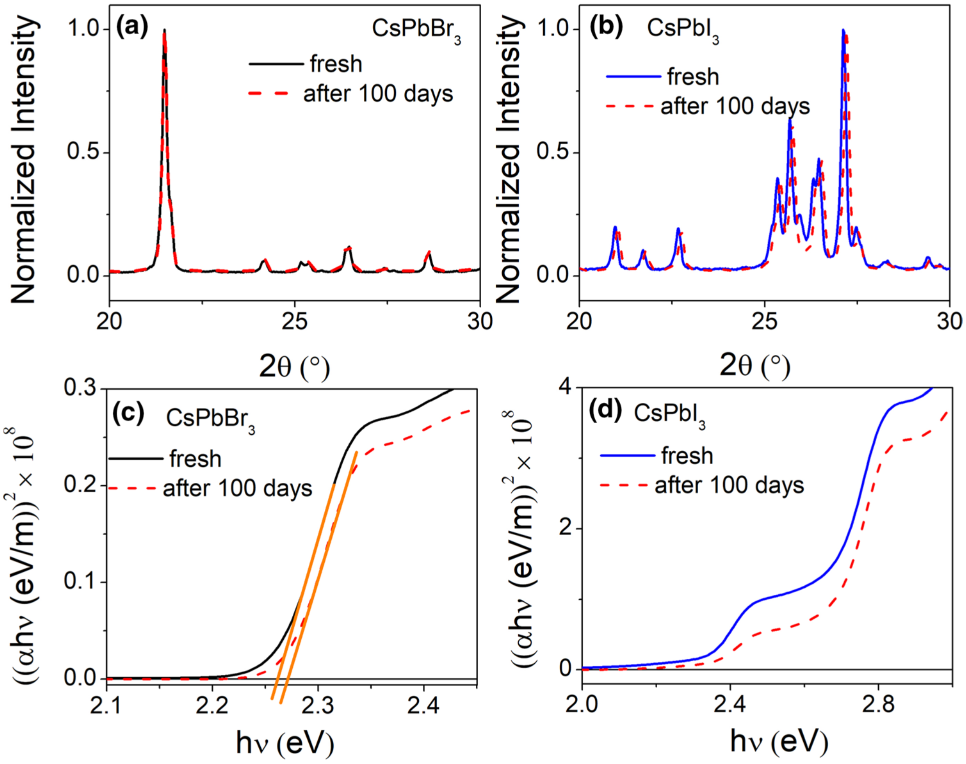

Fig. 11 The comparative normalized XRD patterns in case of **a** CsPbBr$_3$, **b** CsPbI$_3$. The comparative UV absorption spectra in case of **c** CsPbBr$_3$, **d** CsPbI$_3$. [Between 0 day (i.e., freshly prepared sample) and after, 100 days (i.e., aged sample)]

in the agreement with the literature. To verify the stability of sample, we have already shown through thermodynamics that these compounds are thermally stable. Further, the structure of these materials was re-examined from time to time. The comparative between normalized XRD patterns and UV spectra for 0 day (i.e., freshly prepared sample) and after 100 days (i.e., aged sample) are plotted for the two samples and shown in Fig. 11. It is observed that there is no difference in the XRD peak positions for CsPbBr$_3$ (Fig. 11a) whereas, for CsPbI$_3$ (Fig. 11b) the peak positions are slightly shifted towards higher angle. However, the UV absorption spectra in both cases (Fig. 11c, d) show very small increase in the band-gap. Thus, the samples prepared by the cold sintering methods are well stable in structure and absorption spectra with time (for more than 100 days).

Moreover, stability of the samples is also examined in Sun-light exposure, the I–V curves are recorded in the interval of the 30 min over the duration of 3 h in the continuous exposure of AM 1.5G Sun-light (Fig. 12). For both the samples, the current response is observed as soon as AM 1.5G Sun-light switched on, as compared from the dark light and room light. However with the time, no significant degradation is observed for CsPbBr$_3$ but for CsPbI$_3$, the degradation in the AM 1.5G Sun-light was significant as evident from I–V plot for these two samples.

5 Conclusion

The samples CsPbI$_3$ and CsPbBr$_3$ synthesized through cold sintering are crystallized in orthorhombic phase with P*nma* symmetry as verified through structural and electronic studies. The samples synthesized through cold sintering method are favoured thermodynamically. Hence, it’s not intrinsic instability which governs the formation. The band gap energy observed for these two samples synthesized with other significant methods indicates that the value is smallest for the samples prepared by cold sintering. Moreover, structure-optical and thermo-optical correlation has been observed for the synthesized samples. Also, CsPbBr$_3$ is more stable than CsPbI$_3$ on exposure to AM 1.5G sunlight. Hence, we report the cold sintering method as easiest and cheapest method to synthesis perovskite halides in ambient condition.

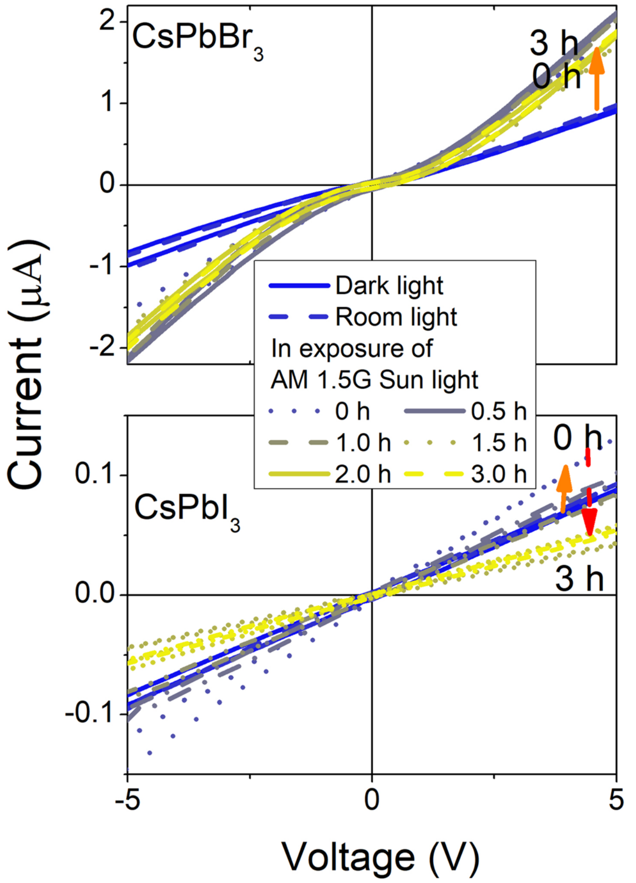

Fig. 12 Current (I)–Voltage (V) plot in different light exposure (dark, room light and AM 1.5 G Sun light) along with current degradation with time (0–3.0 h) in AM 1.5 G Sun light

Acknowledgements One of the authors MK is thankful to UGC (EU-V/2121551193) for JRF.

References

1. T. Markvart, From steam engine to solar cells: can thermodynamics guide the development of future generations of photovoltaics? Wiley Interdiscip. Rev. Energy Environ. **5**(5), 543–569 (2016)
2. P. Kowalczewski, L.C. Andreani, Towards the efficiency limits of silicon solar cells: how thin is too thin? Sol. Energy Mater. Sol. Cells **143**, 260–268 (2015)
3. National Renewable Energy Laboratory, https://www.Nrel.Gov/Pv/Assets/Pdfs/Pv-Efficiencies-07-17-2018.Pdf. Accessed 24 July 2018
4. J. Burschka et al., Sequential deposition as a route to high-performance perovskite-sensitized solar cells. Nature **499**(7458), 316–319 (2013)
5. K. Akihiro Kojima, Y. Teshima, Shirai, T. Miyasaka, Organometal halide perovskites as visible-light sensitizers for photovoltaic cells. J. Am. Chem. Soc. **131**(17), 6050–6051 (2009)
6. N. Yantara et al., Inorganic halide perovskites for efficient light-emitting diodes. J. Phys. Chem. Lett. **6**(21), 4360–4364 (2015)
7. G. Murtaza, I. Ahmad, First principle study of the structural and optoelectronic properties of cubic perovskites CsPbM$_3$(M = Cl, Br, I). Physica B **406**(17), 3222–3229 (2011)
8. M. Maqbool et al., Structural, electronic and optical properties of CsPbX$_3$(X = Cl, Br, I) for energy storage and hybrid solar cell applications. J. Alloys Compd. **705**, 828–839 (2017)
9. W. Zhai et al., Solvothermal synthesis of ultrathin cesium lead halide perovskite nanoplatelets with tunable lateral sizes and their reversible transformation into Cs$_4$PbBr$_6$ nanocrystals. Chem. Mater. **30**(11), 3714–3721 (2018)
10. M. Shekhirev, J. Goza, J.D. Teeter, A. Lipatov, A. Sinitskii, Synthesis of cesium lead halide perovskite quantum dots. J. Chem. Educ. **94**(8), 1150–1156 (2017)
11. H. Liu et al., One-step preparation of cesium lead halide CsPbX$_3$ (X = Cl, Br, and I) perovskite nanocrystals by microwave irradiation. ACS Appl. Mater. Interfaces **9**(49), 42919–42927 (2017)
12. S. Ye, M. Yu, M. Zhao, J. Song, J. Qu, Low temperature synthesis of high-quality all-inorganic cesium lead halide perovskite nanocrystals in open air and their upconversion luminescence. J. Alloys Compd. **730**, 62–70 (2018)
13. D. Zhang, S.W. Eaton, Y. Yu, L. Dou, P. Yang, Solution-phase synthesis of cesium lead halide perovskite nanowires. J. Am. Chem. Soc. **137**(29), 9230–9233 (2015)
14. A. Tejada, S. Braunger, L. Korte, S. Albrecht, B. Rech, J.A. Guerra, Optical characterization and bandgap engineering of flat and wrinkle-textured FA$_{0.83}$Cs$_{0.17}$Pb(I$_{1-x}$Br$_x$)$_3$ perovskite thin films. J. Appl. Phys. **123**(17), 175302 (2018)
15. S. Braunger et al., Cs$_x$FA$_{1-x}$Pb(I$_{1-y}$Br$_y$)$_3$ Perovskite compositions: the appearance of wrinkled morphology and its impact on solar cell performance. J. Phys. Chem. C **122**(30), 17123–17135 (2018)
16. J. Guo, A.L. Baker, H. Guo, M. Lanagan, C.A. Randall, Cold sintering process: a new era for ceramic packaging and microwave device development. J. Am. Ceram. Soc. **100**(2), 669–677 (2017)
17. Y. Liu, Q. Sun, D. Wang, K. Adair, J. Liang, X. Sun, Development of the cold sintering process and its application in solid-state lithium batteries. J. Power Sources **393**, 193–203 (2018)
18. C.D. Wagner, The Nist X-ray photoelctron spectroscopy (XPS) database, p. 76, (1991)
19. C.C. Chusuei, M.A. Brookshier, D.W. Goodman, Correlation of relative X-ray photoelectron spectroscopy shake-up intensity with CuO particle size. Langmuir **15**(8), 2806–2808 (1999)
20. R. Lacomba-Perales, J. Ruiz-Fuertes, D. Errandonea, D. Martínez-García, A. Segura, Optical absorption of divalent metal tungstates: correlation between the band-gap energy and the cation ionic radius. EPL **83**, 37002 (2008)
21. W. Aloui, N. Dhahri, A. Bouazizi, Optical and electrical properties of p-substituted-benzylidenemalononitrile thin films: optoelectronic applications. Superlattices Microstruct. **91**, 302–305 (2016)
22. V. Pawar, P.K. Jha, S.K. Panda, P.A. Jha, P. Singh, Band-gap engineering in ZnO thin films: a combined experimental and theoretical study. Phys. Rev. Appl. **9**(5), 054001 2018
23. F. Urbach, The long-wavelength edge of photographic sensitivity and of the electronic absorption of solids. Phys. Rev. **92**(5), 1324 (1953)
24. I. Guilhon, F. Bechstedt, S. Botti, M. Marques, L.K. Teles, Thermodynamic, electronic, and optical properties of graphene oxide: a statistical ab initio approach. Phys. Rev. B **95**(24), 1–14 (2017)
25. L. Zhang, Y. Cheng, G. Ji, Thermodynamic and optical properties of CuAlO$_2$ under pressure from first principle. J. Wuhan Univ. Technol. Mater. Sci. Ed. **30**(6), 1338–1344 (2015)

26. J. Portier, H.S. Hilal, I. Saadeddin, S.J. Hwang, M.A. Subramanian, G. Campet, Thermodynamic correlations and band gap calculations in metal oxides. Prog. Solid State Chem. **32**(3–4), 207–217 (2004)
27. W. Yao, D. Li, H. Wang, L. Yang, Room-temperature synthesis of Mn^{2+}-doped cesium lead halide perovskite nanocrystals via a transformation doping method. J. Mater. Sci.: Mater. Electron. 3**0**(1), 180–188 (2018)
28. D. Ghosh, M.Y. Ali, D.K. Chaudhary, S. Bhattacharyya, Dependence of halide composition on the stability of highly efficient all-inorganic cesium lead halide perovskite quantum dot solar cells. Sol. Energy Mater. Sol. Cells **185**, 28–35 (2018)
29. G.E. Eperon et al., Inorganic caesium lead iodide perovskite solar cells. J. Mater. Chem. A **3**(39), 19688–19695 (2015)
30. X. Su, J. Zhang, G.E. Bai, Facile synthesis and characterization of $CsPbBr_3$ and $CsPb_2$ Br_5 powders. Bull. Mater. Sci. **41**(2), 1–6 (2018)
31. M. Kulbak, D. Cahen, G. Hodes, How important is the organic part of lead halide perovskite photovoltaic cells? Efficient $CsPbBr_3$ cells. J. Phys. Chem. Lett. **6**(13), 2452–2456 (2015)
32. R.E. Beal et al., Cesium lead halide perovskites with improved stability for tandem solar cells. J. Phys. Chem. Lett. **7**(5), 746–751 (2016)
33. O.N. Yunakova, V.K. Miloslavskii, E.N. Kovalenko, Exciton absorption spectrum of thin $CsPbI_3$ and Cs_4PbI_6 films. Opt. Spectrosc. **112**(1), 91–96 (2012)
34. C.H. Ng et al., Tunable open circuit voltage by engineering inorganic cesium lead bromide/iodide perovskite solar cells. Sci. Rep. **8**(1), 1–9 (2018)